Proceedings of the 2nd International Conference on Software Engineering and Machine Learning
DOI: 10.54254/2755-2721/67/20240685

Research on automated rapid diagnosis of distal radius fractures using X-ray images

Yunpeng Liu[1,5], Yupeng Zhuo[1,6], Ying Wang[2,7,*], Kaifeng Gan[3,8], Dongquan Liu[4,9]

[1]Ningbo University of Technology, Fenghua Road 201, Ningbo, Zhejiang, China
[2]Medical Imaging Research Institute of Henan University, Kaifeng, Henan, 475000, China
[3]Li Huili Hospital Affiliated to Ningbo University, Xingning Road 57, Yinzhou District, Ningbo, Zhejiang, China
[4]Ninghai First Hospital, Taoyuan Middle Road 142, Ninghai County, China

[5]L35633@163.com
[6]ypengzhuo@163.com
[7]hhyyfskwangying@126.com
[8]gankaifeng_nb@163.com
[9]ldq801118@163.com
*corresponding author

Abstract. The primary diagnostic method for distal radius fractures remains conventional X-ray imaging. In emergency situations, rapid assessment and decision-making are often required from non-orthopedic physicians or junior radiologists in the emergency room. Therefore, an accurate and efficient auxiliary diagnostic technology for distal radius fractures is of great significance. This paper combines deep learning with image analysis techniques to propose an effective classification method for types of distal radius fractures. Firstly, an extended U-Net three-level cascade segmentation network is used for precise segmentation of the most critical joint surface and non-joint surface areas for fracture identification. The edge is further optimized using the central pixel image block classification method. Then, fracture identification is performed separately on the joint surface and non-joint surface areas. Finally, based on the classification results of the two types of images, a comprehensive judgment is made to determine normal or ABC fracture types. The experimental X-ray data comes from three tertiary hospitals, with a total of 12,000 images in the training set, 3,000 of each type, and 1,200 images in the test set, 300 of each type. To further demonstrate the generalization performance of the classification experiment, an additional 500 images were added for fracture classification testing, coming from collaborative medical institutions in the United States and Germany. All images were annotated by orthopedic medical experts with more than ten years of experience. The accuracy rates for normal, type A, type B, and type C fractures in the test set were 0.99, 0.92, 0.91, and 0.82, respectively. For orthopedic medical experts, the average recognition accuracy rates were 0.98, 0.90, 0.87, and 0.81. The proposed automatic recognition method overall performs better than experts and can be used for preliminary auxiliary diagnosis of distal radius fractures without expert participation.

Keywords: Deep learning, Medical imaging, Segmentation, Classification, Fracture diagnosis.

DOI: 10.54254/2755-2721/67/20240685

1. Introduction

Distal radius fractures are one of the most common types of fractures in clinical practice. The clinical application of X-ray images has significantly improved the accuracy of diagnosing fracture injury types. X-ray fracture diagnosis essentially falls within the scope of two-dimensional image classification technology. The direct approach is to input the entire raw image into the analysis system, extract features, and use traditional machine learning methods such as support vector machines and random forests to obtain diagnostic classification results [1,2]. Deep learning AI technology, represented by convolutional neural networks, has become mainstream [3-6, 27].

For the diagnosis of distal radius fractures, existing research literature divides the methods into three main categories: (1) Direct classification of X-ray images of the entire palm and wrist area, including the distal radius, primarily focusing on binary classification of fractures and normal [7]. (2) Simultaneous localization or segmentation of the distal radius in X-ray images and classification, also primarily focusing on binary classification of fractures and normal [9-10, 24, 26]. (3) Accurate localization of the distal radius area followed by classification [8, 22, 23, 25]. Although CT is a series of images over time, in actual identification, only a few key clear images from the sequence are selected, so in fracture diagnosis, it is still similar to two-dimensional image processing of X-ray images [11-12].

The above analysis shows that existing domestic and foreign literature does not report precise segmentation and then identification of fractures in X-ray images of the distal radius. They mainly focus on simple binary classification of fractures and normal. Although literature [22] made further improvements to distinguish between type A and BC (as a large category), it still follows a binary classification approach based on object detection, unable to effectively distinguish between type B and C fractures. This paper uses an extended U-Net three-level cascade network structure to perform highly accurate segmentation of joint surface and non-joint surface areas and classifies within the segmented images to comprehensively determine fracture types.

2. Description of Distal Radius Fracture Classification

The term "distal radius" is illustrated in Figure 1. In Figures 1a and 1b, the area marked by the red lines represents the "distal radius" region. In Figure 1b, the green arc indicates the part of the bone that is obscured by adjacent bones, which is also considered part of the posterior "distal radius." Figure 1c provides a more intuitive 3D representation of the "distal radius." The definitions of the "articular surface area" and "non-articular surface area" are shown in Figure 2. The red line delineates the "articular surface area" of the "distal radius," while the green line delineates the "non-articular surface area." The blue line (representing a plane in three-dimensional space) indicates the "metaphysis" area of the "distal radius."

When a fracture occurs only in the "non-articular surface area," including the "metaphysis," it is defined as a "Type A" fracture. The characteristic of a "Type A" fracture is that the fracture line appears only in the "non-articular surface area," as shown in Figure 3a. When a fracture occurs in the "articular surface area" without involving the "metaphysis," it is defined as a "Type B" fracture. The characteristic of a "Type B" fracture is that the fracture line involves the "articular surface area" but does not extend along the entire "metaphysis," as shown in Figure 3b. When a fracture occurs in both the "metaphysis" and the "articular surface area," it is defined as a "Type C" fracture. The characteristic of a "Type C" fracture is that there are fracture lines involving the "articular surface area" and extending along the entire "metaphysis," as shown in Figure 3c.

DOI: 10.54254/2755-2721/67/20240685

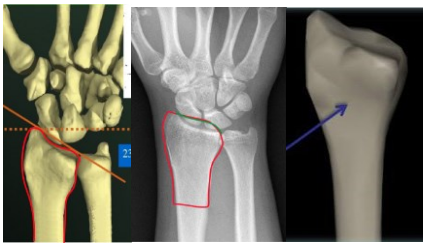

(a) 3D view of the distal radius (b) X-ray (c) Isolated; (a) X-ray image (b) 3D image; (a) Type A (b) Type B (c) Type C

Figure 1. Illustration of the distal radius

Figure 2. Illustration of "articular surface area" and "non-articular surface area"

Figure 3. Illustration of "ABC type" fractures

3. Experimental Environment and Data

The operating system used is Ubuntu 16.04, the development language is Python 3.6.5, and the development environment is Visual Studio Code. Deep learning was conducted using Google's TensorFlow 1.12.0 platform with the corresponding Keras 2.2.5 and cuDNN 7.1.4 libraries. The experiments utilized a single NVIDIA Tesla P100-PCIE GPU device with 12GB of memory, and cuDNN acceleration. The wrist X-ray dataset was obtained from three authoritative tertiary orthopedic hospitals. Each hospital's training and validation dataset included 4,000 images, with 1,000 images each of normal, Type A, Type B, and Type C distal radius fractures. Additionally, each hospital's test set included 400 images, with 100 images of each type, all annotated by orthopedic medical experts with more than ten years of experience. To further demonstrate the generalization performance of the final distal radius fracture classification experiment, in addition to the 1,200 test images from the three Chinese hospitals mentioned above, an additional 500 test images were added solely for the fracture classification testing phase. These images came from collaborative medical institutions in the United States and Germany, with the type proportions approximately 1:1. These images were not used for segmentation, contour optimization, or articular surface area classification training. All images used in the experiment underwent a selection process, with exclusion criteria including: (1) images that were blurred or did not fully display the required area, and (2) images where the required area was obscured by plaster or braces. The selected images ensured that the key area features were clearly visible. For each Chinese hospital, 250 images of each type were randomly selected from the training and validation datasets for segmentation annotation, resulting in a total of 1,000 annotated images for the three regions, and 3,000 images in total from the three hospitals.

4. Research Methods

4.1. Region of Interest Segmentation

4.1.1. Extended U-Net Segmentation Network

An extended U-Net network structure was designed for the segmentation model in this paper, as shown in Figure 4, which includes five encoding and decoding layers. The decoding end uses the upsampling method proposed by Isola et al. [13]. To reduce image loss caused by upsampling, sub-pixel convolution methods [14] were added. Because the "articular surface area" is relatively small, features can be continuously weakened or even disappear during the convolution process. Therefore, an Attention Gate (AG) technique [15] applied to medical imaging was used, which can automatically focus and learn on smaller objects.

DOI: 10.54254/2755-2721/67/20240685

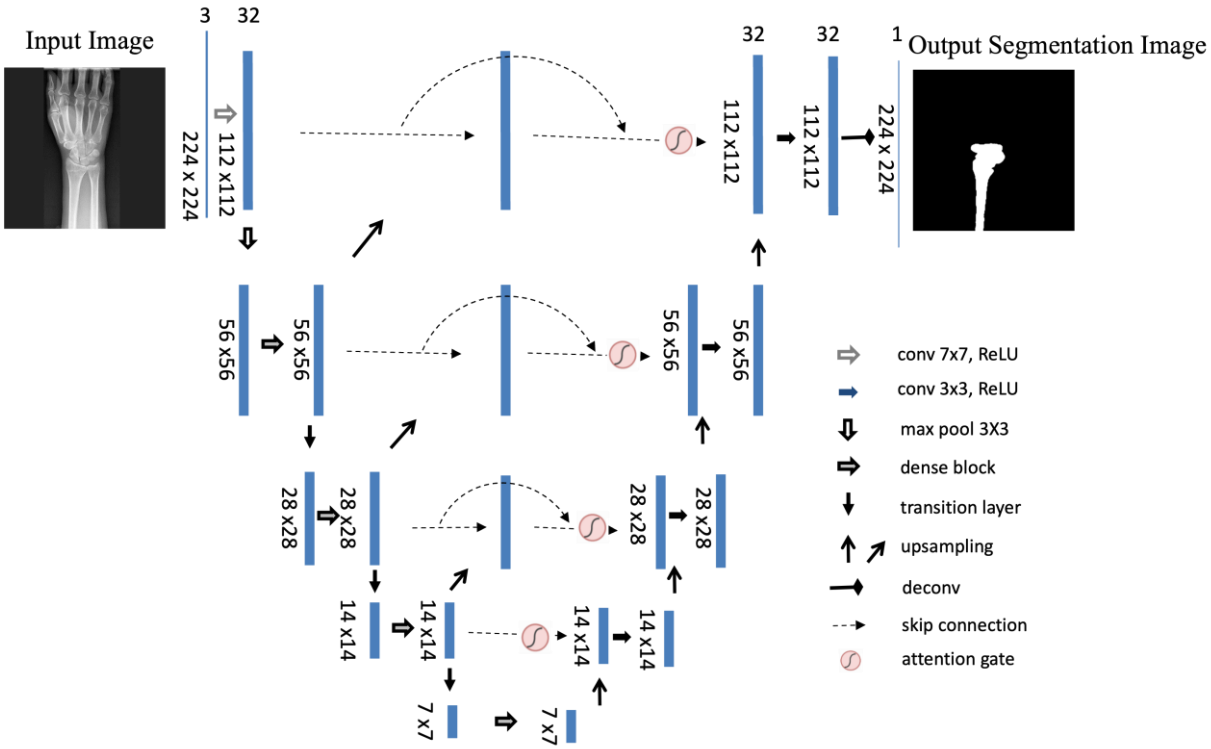

Figure 4. Extending the U-Net network

4.1.2. Three-Level Cascade Segmentation Model

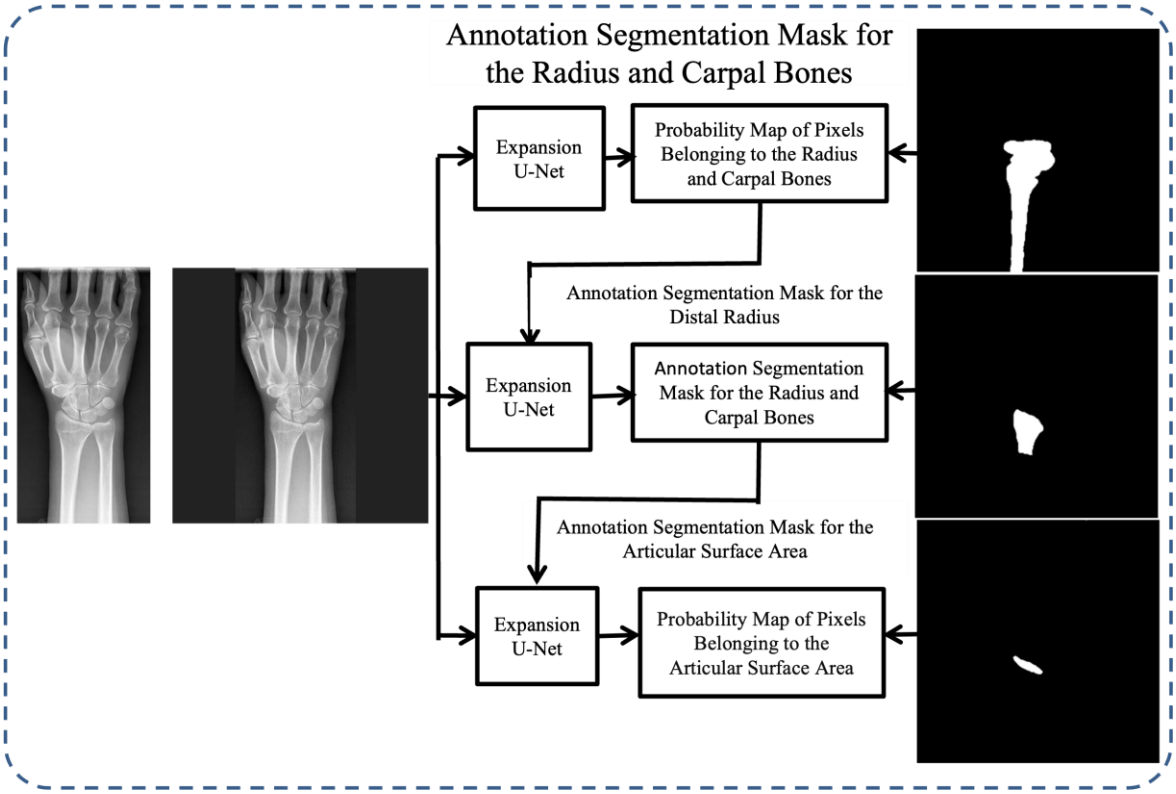

Figure 5. Three-level associative segmentation model

DOI: 10.54254/2755-2721/67/20240685

The end-to-end segmentation network uses three extended U-Net networks to simultaneously segment the "radius and carpal bones," the "distal radius," and the "articular surface area," forming a three-level cascade structure. The upper-level segmented region provides structural and positional constraints on the lower-level segmented region globally. The same convolutional neural network structure is used for the three objects. The difference in segmentation processing between the "distal radius" and "radius and carpal bones" is the addition of the "radius and carpal bones" prediction probability map in the input channel. According to the cascade structure, the "articular surface area" input channel includes the "distal radius" prediction probability map. After cascading the three extended U-Nets, deep learning and prediction can be performed end-to-end.

4.1.3. Experiments and Discussion

(1) Data Preprocessing

The 3000 segmented annotated images are typically rectangular with different widths and heights. Since deep convolutional networks handle square images better, the images need to be adjusted to be square. X-ray images have a black background, so the shorter edge can be padded with the background color value to expand the boundary. This ensures that the wrist object does not deform and remains centered. The same boundary expansion method is used for the mask annotation images used in segmentation training to keep them consistent with the wrist images, and the images are resized to 224×224 pixels.

Five-fold cross-validation was used, with 2400 images for training and 800 images for validation each time. During training, real-time random combination data augmentation operations were performed on the training set, including (1) translation within a 15% range up, down, left, and right, (2) scaling within a 15% range, (3) rotation within 30 degrees, and (4) stretching deformation with a stretch factor range of -5 to 5. Pixels beyond the boundary were filled with black (0). The validation set of 800 images was fixed and not augmented. Images were normalized by dividing all pixel values by 255 to convert them to a 0-1 range.

(2) Training Parameters and Evaluation Criteria

The main training parameters are as follows: batch size of 32, using pixel-wise cross-entropy loss function, Adam optimizer, learning rate set to 0.0001, decay rate set to 0.00001, and epochs set to 120. Training stops if the loss does not decrease after 5 consecutive epochs. The model and corresponding weights with the minimum loss are saved via a callback function. After Adam optimization, the best weights are loaded and further optimized using the SGD optimizer with a learning rate of 0.00001. Final training stops if the loss does not decrease after 10 consecutive epochs, resulting in the optimal segmentation weights. The three regions of interest are segmented simultaneously and evaluated uniformly.

(3) Overall Comparison with Current Advanced Methods

The segmentation performance comparison is shown in Table 1. No papers specifically segmenting the medical image regions described in this paper were found in the known literature. The proposed method was compared with segmentation models that have shown outstanding performance in the medical imaging field in recent years [16-21].

Table 1. Comparison of segmentation performance

Method	sensitivity	PPV	DC
Proposed Method	**0.91±0.02**	**0.94±0.02**	**0.93±0.03**
AA-transunet [16]	0.89±0.03	0.91±0.04	0.90±0.02
SAMM [17]	0.88±0.02	0.90±0.03	0.89±0.02
ResGANet [18]	0.88±0.03	0.91±0.04	0.90±0.03
BlendMask [19]	0.83±0.02	0.89±0.03	0.87±0.03
Transformer [20]	0.80±0.02	0.84±0.03	0.82±0.02
SAM [21]	0.78±0.02	0.82±0.03	0.80±0.02

DOI: 10.54254/2755-2721/67/20240685

As shown in Table 1, the proposed method achieved the highest mean and maximum values for each metric, with maximum sensitivity, PPV, and Dice coefficients of 0.93, 0.96, and 0.96, respectively. Other methods showed poorer segmentation performance, primarily because the texture structure of the "distal radius" and "articular surface area" is very similar to other hand and wrist bone structures, with the main difference being size. Due to the scale-invariant nature of deep learning, false positive objects in non-region-of-interest areas are easily segmented out. The post-processing did not address false positives, leading to significantly reduced final performance. The three-level cascade structure of the proposed method imposes spatial constraints, avoiding any false positive segmentation and demonstrating high precision segmentation.

(4) Display of Typical Segmentation Results

As shown in Figure 6, a typical segmentation result is displayed. The top row from left to right shows the segmentation results of expert annotation, the proposed method, AA-transunet [16], and SAMM [17]. The bottom row from left to right shows the segmentation results of ResGANet [18], BlendMask [19], Transformer [20], and SAM [21]. The red, blue, and yellow lines represent the segmented "radius and carpal bones," "distal radius," and "articular surface area," respectively. Black arrows indicate areas where the segmentation result significantly differs from the actual annotation. It can be seen that the proposed segmentation result is generally consistent with the annotation, while AA-transunet [16], SAMM [17], and ResGANet [18] did not correctly segment the upper curve of the "distal radius" and "articular surface area," potentially losing core features of the "articular surface area" fracture. In addition to the above segmentation issues, BlendMask [19] incorrectly segmented the overlapping area at the upper right of the "distal radius." Transformer [20] and SAM [21] not only had the above two issues but also missed part of the left upper corner of the "radius and carpal bones" segmentation, while incorrectly segmenting the "articular surface area."

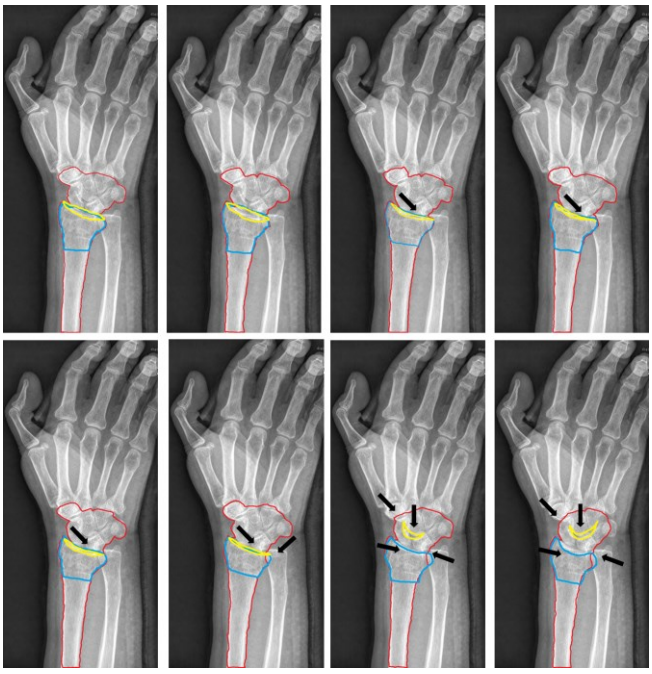

Figure 6. Segmentation and comparison diagram of different methods

4.2. Fracture Detection in Articular Surface and Non-Articular Surface Areas

After precise segmentation, further classification processing is required. For the classification model, both the "articular surface area" and the "non-articular surface area" need to be classified to achieve the final type diagnosis. Both classifications use consistent preprocessing and convolutional neural networks. In the following description, "ROI" will be used to represent either the "articular surface area" or the "non-articular surface area." The ROI area is obtained from the original input image and the

DOI: 10.54254/2755-2721/67/20240685

segmented marked image, and the smallest bounding box of the ROI is expanded to a square using the same boundary expansion algorithm described in the segmentation. Data augmentation includes the following random operations: (1) Gaussian blur with sigma parameter in the range of 0-2, (2) horizontal flipping, (3) rotation within -45 to 45 degrees, and (4) stretching with a stretch factor range of -10 to 10.

This paper uses the EfficientNet-B7 deep network model for binary classification processing, as shown in Figure 7. Taking the "articular surface area" classification as an example, the same method and network model are used for the "non-articular surface area," with differences only in the training data. To achieve higher classification performance, a coarse-to-fine optimization strategy is adopted. The default parameters of the Adam method are used for optimization. After the performance can no longer be improved with Adam, the weights are adjusted using the SGD optimization method to achieve better classification performance.

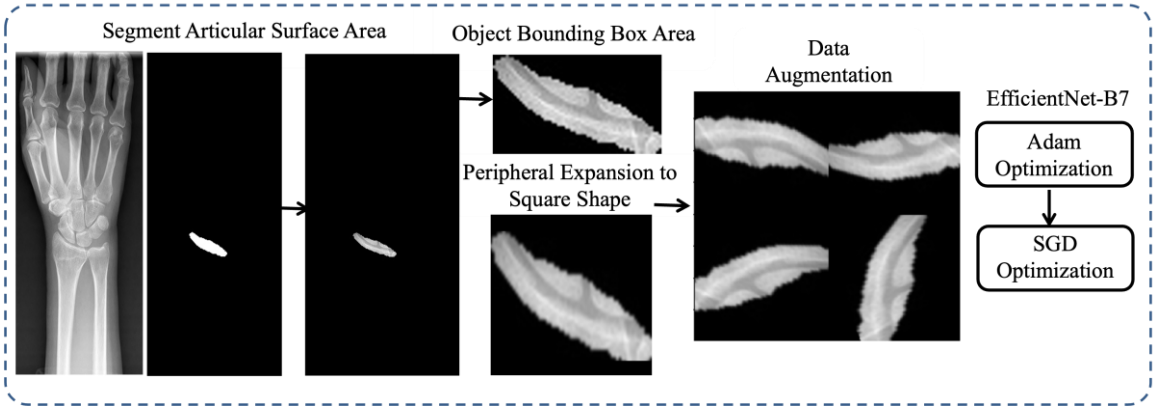

Figure 7. Training frame of fracture judgment model

Experiments compared the model with AmoebaNet-A, NASNet-A, and ResNeXt-101 models. As shown in Tables 2 and 3, the EfficientNet-B7 model achieved the best classification performance. Due to the more prominent texture features of fractures in the "non-articular surface area," the overall accuracy is higher.

Table 2. "Articular Surface Area" Classification Comparison

CNN Model	Validation Accuracy
EfficientNet-B7	**0.94±0.05**
AmoebaNet-A	0.92±0.06
NASNet-A	0.91±0.05
ResNeXt-101	0.91±0.06

Table 3. "Non-Articular Surface Area" Classification Comparison

CNN Model	Validation Accuracy
EfficientNet-B7	**0.96±0.02**
AmoebaNet-A	0.95±0.02
NASNet-A	0.94±0.02
ResNeXt-101	0.94±0.03

To further explain the interpretability of the classification model, the Class Activation Map method was used to visualize the recognized features in the image as heat maps. Dark red indicates the most significant features, while dark blue indicates the least significant. Only the "distal radius" region of interest is shown, as illustrated in Figure 8. Among them, (a) shows a more obvious fracture, and (b), (c), and (d) show minor fractures and overlapping radius cases. The fracture area is marked with a red ellipse, and the overlapping radius area is marked with a yellow rectangle. The heat maps indicate that

DOI: 10.54254/2755-2721/67/20240685

although radius overlap interferes with fracture recognition in the articular surface area, both obvious and minor fractures in the articular and non-articular areas still show the most significant colors. Because the segmentation accuracy of the radius edge is high, the overlapping area is highlighted due to its positional and grayscale differences from other areas, allowing the deep learning model to learn the features better and distinguish them from actual fracture areas. For the human eye, minor fractures are not apparent in texture feature distribution. However, the deep learning model can accurately learn the texture feature differences between fracture and normal areas using the parameter settings and training methods proposed in this paper.

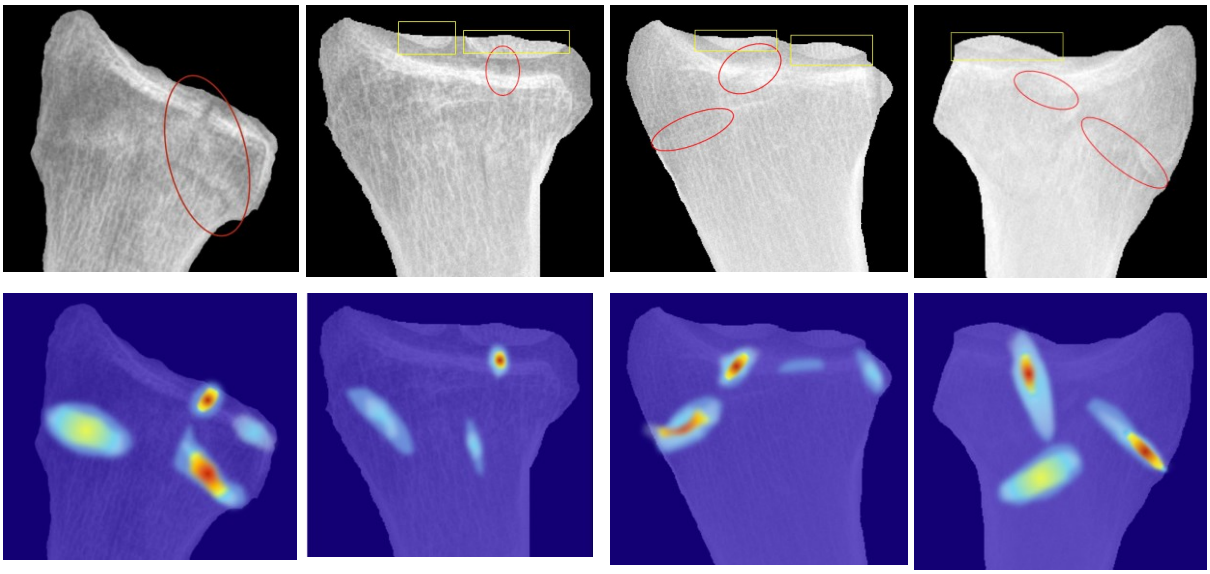

(a) Obvious fracture (b) Minor fracture with radius overlap 1 (c) Minor fracture with radius overlap 2 (d) Minor fracture with radius overlap 3

Figure 8. Visualization of fracture activation features

4.3. Distal Radius Fracture Type Diagnosis

4.3.1. Diagnosis Method

As shown in Figure 9, first, the segmentation model is used to obtain the segmented regions of the "distal radius" and "articular surface area." Second, the "non-articular surface area" segmentation region is obtained by region subtraction. Next, the minimum bounding box of the object is obtained in the original image, the boundary is expanded to a square, and the size is scaled to the classification model requirements. Finally, two classification models are used to predict the two regions separately, and the fracture type is comprehensively determined.

DOI: 10.54254/2755-2721/67/20240685

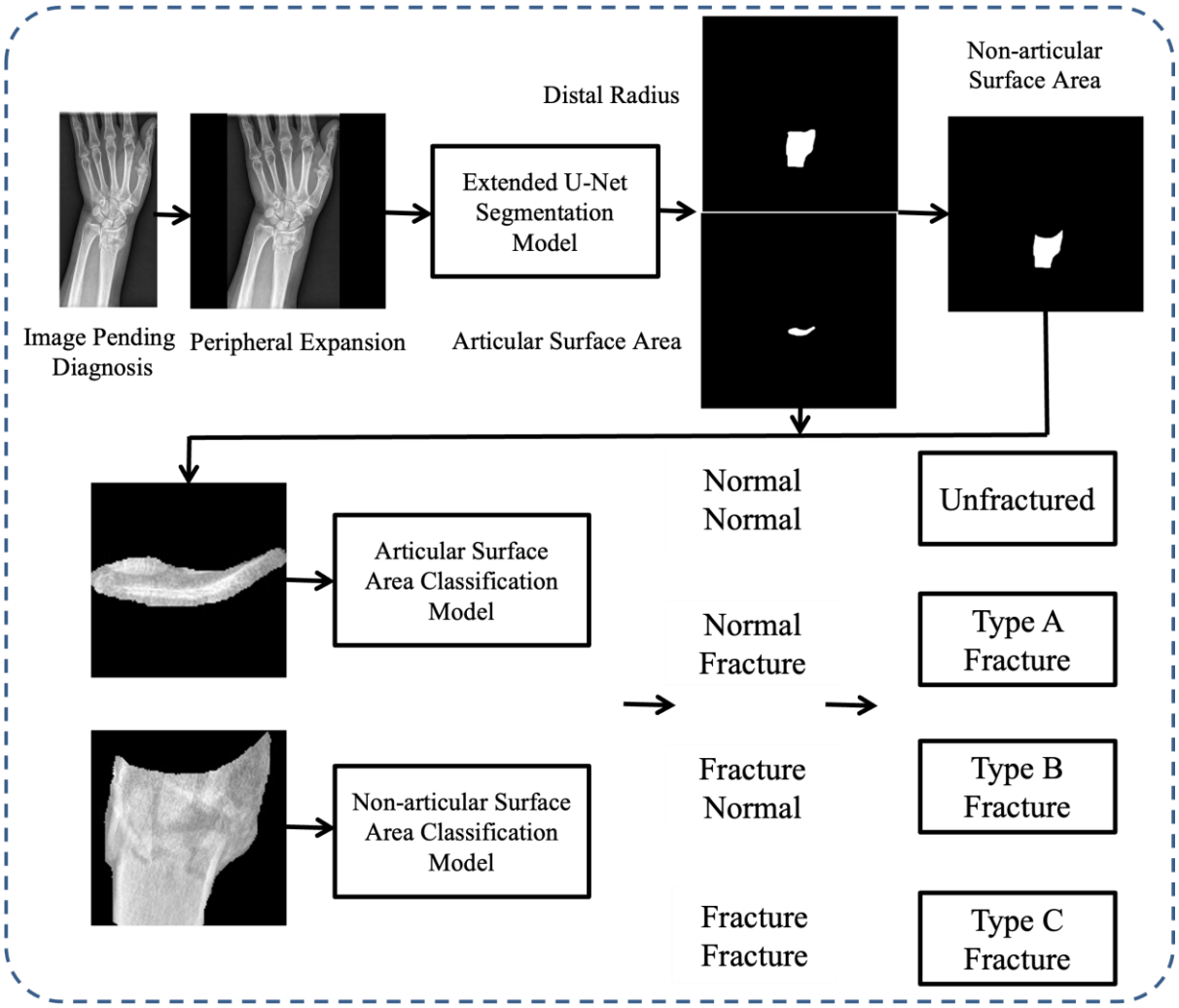

Figure 9. Frame diagram of typing diagnosis

4.3.2. Experiments and Discussion

The ultimate goal of the three models described above is to correctly type fractures. The 12,000 annotated X-ray images are used for the aforementioned segmentation and classification training. The trained deep learning models are tested on 1,700 new patient images (1,200 domestic and 500 foreign). On the one hand, the results are compared with the four-category classification effect directly using the overall image. The model is trained directly with 12,000 expert-annotated data. On the other hand, the results are compared with the average diagnosis results of three experts.

Table 4. Comparison of Typing Results in Test Sets

Method	Normal	Type A	Type B	Type C
Proposed Method	**0.99 0.99 0.99 0.99**	**0.92 0.93 0.92 0.92**	**0.91 0.93 0.91 0.91**	**0.82 0.80 0.82 0.79**
Expert Diagnosis	0.98 0.98 0.98 0.98	0.90 0.92 0.90 0.90	0.87 0.90 0.88 0.87	0.81 0.82 0.81 0.80
EfficientNet-B7	0.93 0.90 0.93 0.88	0.80 0.81 0.79 0.76	0.75 0.80 0.75 0.73	0.66 0.70 0.66 0.64
AmoebaNet-A	0.93 0.95 0.93 0.90	0.75 0.76 0.75 0.72	0.72 0.77 0.71 0.73	0.62 0.62 0.63 0.60
NASNet-A	0.92 0.93 0.92 0.90	0.71 0.73 0.71 0.72	0.70 0.73 0.70 0.66	0.61 0.60 0.61 0.58
ResNeXt-101	0.91 0.91 0.91 0.90	0.71 0.72 0.71 0.69	0.71 0.75 0.71 0.72	0.60 0.58 0.60 0.58

In Table 4, each cell contains four metrics. From left to right, they represent accuracy, precision, recall, and F-score. The proposed method's final typing diagnosis results are slightly better than the

DOI: 10.54254/2755-2721/67/20240685

average diagnosis of experts, indicating the algorithm's good ability to recognize minor fractures and overlapping radius areas.

5. Conclusion

This paper proposes an intelligent and automated injury classification method for diagnosing distal radius fractures using X-ray images. By employing a three-level cascade segmentation technique, it achieves precise segmentation of the most critical areas for fracture identification, namely the articular surface and non-articular surface areas. On this basis, it accurately classifies normal, Type A, Type B, and Type C fractures, with an average recognition rate slightly higher than that of orthopedic experts. This method can assist doctors in accurately diagnosing distal radius fractures and has already been integrated into the medical imaging research platform of collaborating enterprises. It is currently undergoing trial use in several tertiary hospitals in Ningbo.

Funding

This research was supported by the Ningbo Natural Science Foundation (2023J182), the Ningbo Medical Science and Technology Plan Project (No. 2021Y71), the Ningbo Public Welfare Fund Project (No. 2022S048), the Ninghai County Social Development Science and Technology Plan Project (No. 2106), the Zhejiang Provincial Natural Science Foundation (Grant No. LQ21H060002), the Henan Provincial Health Commission Joint Construction Project (LHGJ20230442), and the Kaifeng City Science and Technology Bureau Research Project (2303052).

References

[1] Adigun O, Ronke B, Mohammed R, et al. Detection of fracture bones in X-ray images categorization[J]. Journal of Advances in Mathematics and Computer Science, 2020, 35: 1-11.
[2] Hržić F, Štajduhar I, Tschauner S, et al. Local-entropy based approach for X-ray image segmentation and fracture detection[J]. Entropy, 2019, 21(4): 338.
[3] Kitamura G. Deep learning evaluation of pelvic radiographs for position, hardware presence and fracture detection[J]. European Journal of Radiology, 2020, 130: 109139.
[4] Guan B, Zhang G, Yao J, et al. Arm fracture detection in X-rays based on improved deep convolutional neural network[J]. Computers & Electrical Engineering, 2020, 81: 106530.
[5] Meena T, Roy S. Bone fracture detection using deep supervised learning from radiological images: a paradigm shift[J]. Diagnostics, 2022, 12(10): 2420.
[6] Guan B, Yao J, Wang S, et al. Automatic detection and localization of thighbone fractures in X-ray based on improved deep learning method[J]. Computer Vision and Image Understanding, 2022, 216: 103345.
[7] Kim D H, MacKinnon T. Artificial intelligence in fracture detection: transfer learning from deep convolutional neural networks[J]. Clinical radiology, 2018, 73(5): 439-445.
[8] Krogue J D, Cheng K V, Hwang K M, et al. Automatic hip fracture identification and functional subclassification with deep learning[J]. Radiology: Artificial Intelligence, 2020, 2(2): e190023.
[9] Raisuddin A M, Vaattovaara E, Nevalainen M, et al. Critical evaluation of deep neural networks for wrist fracture detection[J]. Scientific Reports, 2021, 11(1): 1-11.
[10] Hardalaç F, Uysal F, Peker O, et al. Fracture detection in wrist X-ray images using deep learning-based object detection models[J]. Sensors, 2022, 22(3): 1285.
[11] Lee K M, Lee S Y, Han C S, et al. Long bone fracture type classification for limited number of CT data with deep learning[C]//Proceedings of the 35th Annual ACM Symposium on Applied Computing. ACM, 2020: 1090-1095.
[12] Warin K, Limprasert W, Suebnukarn S, et al. Maxillofacial fracture detection and classification in computed tomography images using convolutional neural network-based models[J]. Scientific Reports, 2023, 13(1): 3434.

DOI: 10.54254/2755-2721/67/20240685

[13] Isola P, Zhu J Y, Zhou T H et al. Image-to-image translation with conditional adversarial networks[C]//Proceedings of 2017 IEEE Conference on Computer Vision and Pattern Recognition. IEEE, 2020:5967-5976.
[14] Shi W Z, Caballero J, Huszár F, et al. Real-time single image and video super-resolution using an efficient sub-pixel convolutional neural network[C]//Proceedings of 2016 IEEE Conference on Computer Vision and Pattern Recognition. IEEE, 2016: 874-1883
[15] Oktay O, Schlemper J, Le Folgoc L L, et al. Attention u-net: learning where to look for the pancreas[OL]. arXiv, 2018, 1804.03999.
[16] Yang Y, Mehrkanoon S. Aa-transunet: Attention augmented transunet for nowcasting tasks[C]//International Joint Conference on Neural Networks. IEEE, 2022:01-08.
[17] Ma J, Wang B. Segment anything in medical images[OL]. arXiv preprint, 2023, 2304.12306.
[18] Cheng J, Tian S, Yu L, et al. ResGANet: residual group attention network for medical image classification and segmentation[J]. Medical Image Analysis, 2022, 76: 102313.
[19] Chen H, Sun K, Tian Z, et al. BlendMask: top-down meets bottom-up for instance segmentation[C]//Proceedings of the IEEE/CVF conference on computer vision and pattern recognition. IEEE, 2020:8573-8581.
[20] Zheng S, Lu J, Zhao H, et al. Rethinking semantic segmentation from a sequence-to-sequence perspective with transformers[C]//Proceedings of the IEEE/CVF conference on computer vision and pattern recognition. IEEE, 2021:6881-6890.
[21] Kirillov A, Mintun E, Ravi N, et al. Segment anything[OL]. arXiv preprint, 2023, 2304.02643.
[22] Min H, Rabi Y, Wadhawan A, et al. Automatic classification of distal radius fracture using a two-stage ensemble deep learning framework[J]. Phys Eng Sci Med, 2023, 46(2): 877-886.
[23] Gan K, Xu D, Lin Y, et al. Artificial intelligence detection of distal radius fractures: a comparison between the convolutional neural network and professional assessments[J]. Acta Orthop, 2019, 90(4): 394-400.
[24] Anttila T T, Karjalainen T V, Mäkelä T O, et al. Detecting Distal Radius Fractures Using a Segmentation-Based Deep Learning Model[J]. J Digit Imaging, 2023, 36: 679–687.
[25] Suzuki T, Maki S, Yamazaki T, et al. Detecting Distal Radial Fractures from Wrist Radiographs Using a Deep Convolutional Neural Network with an Accuracy Comparable to Hand Orthopedic Surgeons[J]. J Digit Imaging, 2022, 35: 39–46.
[26] Yahalomi E, Chernofsky M, Werman M. Detection of Distal Radius Fractures Trained by a Small Set of X-Ray Images and Faster R-CNN[J]. Advances in Intelligent Systems and Computing, 2019, vol 997.
[27] Kuo R Y L, Harrison C, Curran T A, et al. Artificial Intelligence in Fracture Detection: A Systematic Review and Meta-Analysis[J]. Radiology, 2022, 304(1): 50-62.